Microchimica Acta (2021) 188: 230
https://doi.org/10.1007/s00604-021-04884-0

ORIGINAL PAPER

Perylene diimide/MXene-modified graphitic pencil electrode-based electrochemical sensor for dopamine detection

Umay Amara[1,2] · Muhammad Taqi Mehran[3] · Bilal Sarfaraz[3] · Khalid Mahmood[2] · Akhtar Hayat[1] · Muhammad Nasir[1] · Sara Riaz[4] · Mian Hasnain Nawaz[1]

Received: 22 February 2021 / Accepted: 1 June 2021 / Published online: 12 June 2021

Abstract

The synthesis of novel architecture comprising perylene diimide (PDI)-MXene ($Ti_3C_2T_X$)-integrated graphitic pencil electrode for electrochemical detection of dopamine (DA) is reported. The good electron passage between PDI-MXene resulted in an unprecedented nano-adduct bearing enhanced electrocatalytic activity with low-energy electronic transitions. The anionic groups of PDI corroborated enhanced active surface area for selective binding and robust oxidation of DA, thereby decreasing the applied potential. Meanwhile, the MXene layers acted as functional conducive support for PDI absorption via strong H-bonding. The considerable conductivity of MXene enhanced electron transportation thus increasing the sensitivity of sensing interface. The inclusively engineered nano-adduct resulted in robust DA oxidation with ultra-sensitivity (38.1 $\mu A \mu M^{-1} cm^{-2}$), and low detection limit (240 nM) at very low oxidation potential (−0.135 V). Moreover, it selectively signaled DA in the presence of physiological interferents with wide linearity (100–1000 μM). The developed transducing interface performed well in human serum samples with RSD (0.1 to 0.4%) and recovery (98.6 to 100.2%) corroborating the viability of the practical implementation of this integrated system.

Keywords MXene · Perylene diimide · Electrochemical sensor · Low oxidation potential · Dopamine · Serum sample analysis

Introduction

In recent years, the rapid promotion of improved health induced the ubiquitously push in mechanical infrastructures and microelectronic sensing devices [1]. Dopamine (DA) is renowned as a critical neurotransmitter [2]. Society is paying a dreadful price due to maladaptive mental disorders and ailments caused by DA dysfunctions [3] like Parkinson's syndrome, hyperactive disorder, Alzheimer's disease, and depression [4] .Although research on electrochemical DA sensors has made great progress with good quantitative readout in nanosystems and microsystems [5], still there are major analytical challenges associated with selectivity and sensitivity of DA detection. The low concentration of DA in biological fluids compared to the coexisting species poses great challenge. Therefore, full-range DA diagnostics requires a sensing interface to precisely distinguish and detect signals in complex biological systems to specifically output corresponding DA signals [6]. To accomplish the desired trait, a sensor must pose higher sensitivity and should manifest long-term mechanical stability. Carbon-based electrodes have been regarded as the best choice for DA oxidation [7]. However, the large overpotential, typically around 0.3 V vs Ag/AgCl at carbon electrodes, made quantitative analysis far more difficult owing to the oxidation of interferent ascorbic acid [8]. One promising approach to decrease the operating potential is to use the redox mediators on electrode interface, which can enhance electron transfer kinetics between the DA and electrode [9]. On the

✉ Khalid Mahmood
khalidmahmood@bzu.edu.pk

✉ Mian Hasnain Nawaz
mhnawaz@cuilahore.edu.pk

[1] Interdisciplinary Research Centre in Biomedical Materials (IRCBM), COMSATS University Islamabad, Lahore Campus, Lahore 54000, Pakistan

[2] Institute of Chemical Sciences, Bahauddin Zakariya University, Multan 60800, Pakistan

[3] School of Chemical and Materials Engineering (SCME), National University of Sciences and Technology (NUST), Islamabad H-12, Pakistan

[4] Department of Chemistry, COMSATS University Islamabad, Lahore Campus, Lahore 54000, Pakistan

other hand, novel microstructures with defined morphologies have demonstrated enhanced sensitivity of these sensing interfaces. Nevertheless, it is still very expensive and hard to fabricate sensitive sensors with low detection limit (S/N ratio) especially at lower oxidation potential, and more efforts are required to incorporate desirable features into such devices.

Recently, MXene ($Ti_3C_2T_X$), a member of 2D metal carbides, nitrides, and carbonitrides (with formula $M_{n+1}X_nT$, where M represents early transition metal, X is carbon and or nitrogen, while T is surface functional groups, i.e., =O, –OH, and –F) has emerged as stack-like laminated material with paradigm qualities [10, 11]. MXene can be synthesized by selectively etching the "A" layer from MAX phases and has great potential for developing sensitive sensing interfaces due to tunable electronic properties and easily adjustable bandgap owing to altering surface functional group or layers number [12–15]. Importantly, the remarkable conductivity and large surface area along a greater number of hydrophilic functional groups make the MXene more accessible to analytes for sensing applications [16]. However, the direct use of MXene sheets is less favorable because of poor stability in colloidal solutions resulting from the spontaneous oxidation of MXene in the air [17, 18]. The oxidation generally begins at defects or edges with the formation of TiO_2 nanocrystals that lead to low electrode stability and limit the working potential range particularly in electrochemical applications.

To circumvent this shortcoming, MXene could be assembled with other nanomaterials to provide desirable stability in wide potential bounds with an improved electroanalytical response. However such assembling of MXene sheets into stable nanoarchitecture is a difficult process and it could compromise some of their intrinsic properties. Therefore, the development of MXene-based sensors without sacrificing these inherent characteristics remains a challenge to the scientific community. We tried to combat this challenge by exploiting perylene diimide (PDI) which proved to be a promising material in many electrochemical applications [19, 20]. The rigid planer backbone of PDI leverage the charge transport mobility and improve electronic conjugation due to π-π interactions among redox-active quinone functionalities [21–23] Additionally, tailorable chemical properties, owing to imide functionalization with charged or hydrophilic moieties in the bay region [24] and pronounced thermal, photochemical, and substantial air stability along with inimitable self-assembly performance, make them an ideal candidate for sensing applications. Making use of the copious surface functional moieties (F, O, H) of MXene sheets, H bonds are likely to be formed between imide nitrogen (–NH) of PDI and MXene sheets. This synergy of orderly stacked MXene and PDI resulted in a scaled-up hierarchal microstructure-based sensing interface with plentiful interfacial interactions. These interactive forces unified adjacent building units, which eventually could enhance stability and biocompatibility with robust response even at lower oxidation potential.

Herein, by exploiting the intrinsic properties of pristine MXene sheets and PDI, we successfully self-assembled these adducts followed by anchoring them onto the graphitic pencil electrode to give stable nanostructures (PDI-MXene/GPE). Furthermore, the adherence between fabricated materials resulted in a highly stable sensing interface with superior sensitivity, lower working potential with linear bounds, and good limit of detection. Moreover, the negatively charged carboxyl group of PDI attracts positively charged DA through π-π stacking which increased the selectivity and electrocatalytic efficacy of the developed sensor. The integrated sensor also demonstrated a good response in human serum samples with recovery of (98.6 to 100.2%), corroborating the clinical applications for DA homeostasis.

Experimental section

Chemicals

Perylene diimide, potassium ferrocyanide ($K_4Fe(CN)_6$), potassium ferricyanide ($K_3Fe(CN)_6$), phosphate buffer saline (PBS), MAX phase (Ti_3AlC_2), hydrofluoric acid (HF), glucose, fructose, ascorbic acid, uric acid, urea, sodium chloride, and potassium chloride were purchased from Sigma-Aldrich and were used as received. Human serum samples were collected from a local hospital and stored at 4°C. The donors of serum samples have average age (25–40), gender (male), and health condition (moderate).All other chemicals were of analytical grade and solutions were prepared from doubly distilled water by Milli-Q water purifying system at room temperature.

Instrumentation

Electrochemical measurements were performed at AMEL 2553, potentiostat/galvanostat equipped with ZPulse software. A conventional three-electrode system containing graphitic pencil electrode as a working electrode, Ag/AgCl/Sat. KCl electrode as a reference electrode with standard potential of (E=+0.197 V saturated), and platinum-based counter electrode. Electrochemical impedance spectroscopy (EIS) measurements were performed in the presence of 5 mM ferro/ferri solution (1:1). Eppendorf 5430 R centrifuge with working radius of 8 cm was used for centrifugation of MXene. UV-Visible spectra were recorded on Perkin Elmer UV-Vis spectrometer Lambda 25 in the range of 800–200 nm. Fourier transform infrared (FTIR) spectroscopy was performed on Thermo scientific Nicolet 6700 in ATR mode to analyze the functionalities present in the composite and pristine materials. The surface morphologies of modified electrodes were studied by atomic force microscopy (AFM) at Park Systems AFM XE7 in non-contact mode and scanning electron microscopy (SEM) at TESCAN VEGA 3. Working interface, i.e.,

graphitic pencil electrode, was manually cut and used for microscopic analysis. All the measurements were performed at room temperature.

Preparation of MXene

The MXene was prepared from MAX phase (Ti_3AlC_2) treated with 40% aqueous solution of hydrofluoric acid (HF) as etchant. For a typical reaction, 10 mL of 50% HF was added to an equal amount of deionized water in a polypropylene bottle. Two grams of MAX phase powder was then slowly added to the HF solution under magnetic stirring and the mixture was heated at 35–40 °C for 8 h with continuous stirring. After the reaction, the reaction mixture was cooled to room temperature and washed with centrifugation at 4000 revolutions per minute of rotor (RPM) or 1431 relative centrifugal force (RCF) or g forces (using Eppendorf 5430 R centrifuge with working radius of 8 cm) in deionized water. To get the desired product, continues washing of the reaction mixture was performed with deionized water and ethanol to maintain the pH at 6, followed by vacuum drying at 80 °C for 24 h [25].

Preparation of PDI-MXene adduct

PDI-MXene adduct was prepared by ultra-sonication of 1:1 mixture of MXene (1mg/mL) and PDI (1mg/mL) for 10 min [20, 26]. Ultra-sonication-induced acoustic cavitation improved the dispersion stability of assembling molecules and eventually facilitated π-π interactions between them, leading to the stable adduct formation [27].

Electrochemical studies

The obtained PDI-MXene nano-adduct was then used to modify the graphitic pencil electrodes (GPE) as fabrication step for the development of DA detection system. Before modification of PDI-MXene adduct, the working interface of GPE was washed with doubly distilled water. GPE was chosen as a working interface (2 mm) owing to economic viability, easy availability, and minimal pretreatment requirement. Besides this, its graphitic surface sp^2-hybridized carbon facilitates easy fabrication and good adsorption without any binder. To deposit the prepared nano-adduct on the working electrode surface, typically 5 μL of PDI-MXene was drop-casted on the working surface of GPE and dried at ambient temperature. After complete drying, the modified GPE was transferred into the electrochemical cell system and tested under different concentrations of DA in PBS with cyclic voltammetry (CV) in the potential range of −0.8 –0 V. The spikes of DA were added after every 50 s in an electrochemical cell containing 20 mL PBS to analyze the response of fabricated electrode towards different concentrations of DA. All the measurements were performed at scan rate of 50 mV/s.

Results and discussions

Morphological, structural, and compositional analysis of synthesized materials

The morphological structure of MXene was characterized by scanning electron microscopy and the images elucidate the successful formation of MXene sheets. The images revealed that Al is etched from the MAX phase leading to the formation of stacked MXene sheets with fine accordion-like morphology as shown in Fig. 1 (A & C). In particular, the edges of the MXene sheets are flat rather than curved depicting the good interaction (H bonding) between MXene sheets [28]. Furthermore, the interlayer spacing between MXene sheets provided a more available area for chemical activity than in the three-dimensional MAX phase. The average thickness of the MXene flake is found to be 1.5 nm which is in good agreement with the reported literature [29–31]. Likewise, it is envisioned from Fig. 1 (B) that PDI has been enwrapped homogenously on MXene flakes via H bonding and π-π stacking. This strong interaction generates a stable interface with massive active sites for DA adsorption and enhances catalytic activity.

Figure 1 (D) depicts the XRD pattern of synthesized MXene and PDI-MXene architectures. Peaks (002), (004), (006), (008), (104), and (105) at 2 value of 9.05, 18.37, 27.75, 34.31, 38.97, and 41.66, respectively, correspond to MXene peaks as shown in Fig. 1 D(a). The (002) and (004) peaks were shifted down in MXene from MAX phase (Ti_3AlC_2), from 9.5 to 9.05 and 19.1 to 18.37, respectively, as perceived from Fig. 1 D(b). This shift was due to an increase in interlayer space between MXene stacks after exfoliation [28], while peak (008) moved from 34 to 34.31 and the intensity of (104) peak was much reduced. However, diffraction peaks at (002), (004), (006), (008), (104), and (105) were shifted towards higher 2 at 9.95, 19.3, 29.5, 35.25, 40.5, and 43.75 as shown in Fig. 1 D(c). This shift in scanning angle was due to hydrogen bonding between PDI and MXene sheets. The rest of the prominent diffraction peaks at 13.45, 14.85, and 32.45 corresponds to the PDI molecule.

The surface morphology of MXene and PDI-decorated MXene sheets have also been evaluated via AFM as shown in fig S1. The topological height of the MXene sheets was found to be approximately 110 nm as revealed in fig S1(A). These findings are in good agreement with the reported literature [32, 33]. However, the topological height increased to 0.18 μm after the addition of PDI nanoparticles into MXene as revealed in fig S1(B). This increase elucidates the formation of nano-adduct with good interactive forces between exemplified materials. AFM also reveals that MXene has a rough surface with root-mean-square roughness (Rq) of 75 nm. However, the integrated interface PDI-MXene bears large-sized homogenized particles with a roughness of 156 nm.

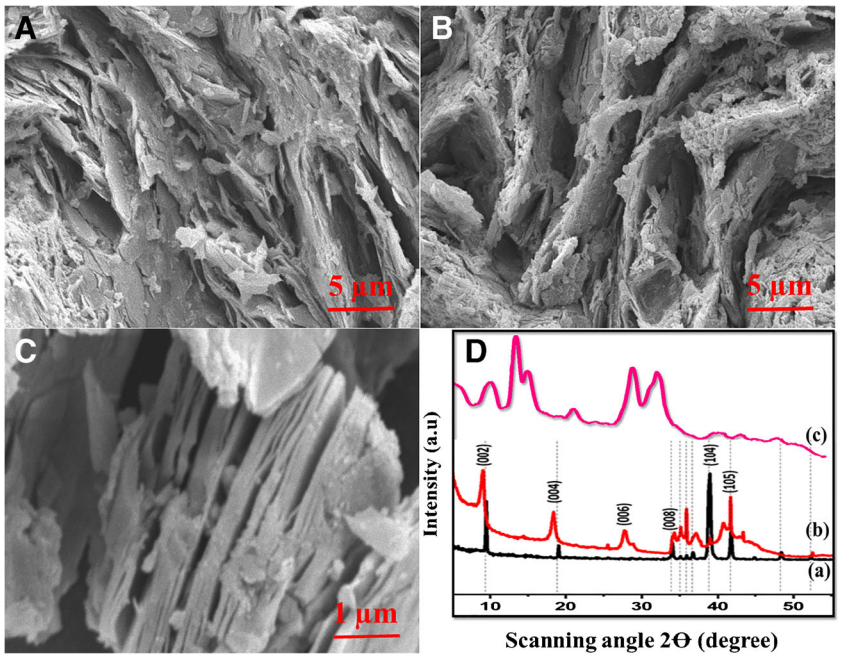

Fig. 1 SEM image of MXene (**A**) and PDI-MXene (**B**), with high-resolution SEM of MXene (**C**); XRD pattern (**D**) of (a) Ti_3AlC_2 MAX phase, (b) MXene, and (c) PDI-MXene

The much higher roughness compared to previously reported MXene-based sensors elucidate the excellent surface activity of integrated nano-catalyst [34]. These bulky sized particles with higher surface roughness and defects ultimately endow massive active surface sites for dopamine absorption which eventually resulted in increased electrocatalytic efficiency for DA oxidation.

The surface defects of MXene before and after assembling with PDI have been evaluated via Raman spectroscopy. The peak at 1315 cm^{-1} corresponds to the surface disorders and defects in the graphitic matrix and is named as D band. Moreover, another peak at 1432 cm^{-1} can be envisioned from Fig S2 (a) which corresponds to sp^2 carbon of the graphitic skeleton and was labeled as G band. The (I_D/I_G) was found to be 1.01 for MXene. The low-intensity peaks and ratio indicate the presence of a fewer amount of amorphous carbon content due to the scarcity of oxygen source. The scarcity in oxygen content is due to the short duration of the synthetic process [35]. However, the D and G bands become very strong and intense after coupling of MXene with PDI molecules as can be envisioned from fig S2 (b). The notable increase in I_D/I_G ratio (1.12) could be attributed to the greater degree of the disorder compared to pristine MXene sheets. These results were also validated from microscopic studies of these adducts via AFM and SEM. Furthermore, a shift in D and G bands has also been witnessed in the XRD pattern of PDI-MXene, as shown in Fig. 1 D(c) that validated the existence of interacting forces in integrated nano-adduct.

UV-Vis was performed to illustrate the PDI-MXene nano-adduct formation and results are shown in fig S3(A). PDI has shown multiple sharp and intense absorption peaks in the range of 200–800 nm. The absorption peaks observed at wavelengths of 266, 500, and 608 nm could be attributed to the n-π* and π-π* electronic transitions as revealed in fig S3 A(a). MXene has shown a small absorption peak at 246 nm which could be imputed to the occurrence of surface terminations [36] as shown in fig. S3 A(b). In contrast to both the parent molecules, PDI-MXene exhibited a lower energy transition at four absorption peaks, i.e., 246, 266, 501, and 608 nm, which could be attributed to the charge transfer state and formation of PDI-MXene nano-adduct [37] as depicted in fig S3 A(c).

Band gaps of pristine materials and nano-adduct were premeditated using Tauc and Davis-Mott relationship that can be extracted from UV-Vis data as displayed in equation S2 [38]. The FTIR spectroscopy was also applied to explore the changes in functionalities of parent molecules and to interpret nano-adduct formation as shown in fig S4.

Electrochemical investigation of modified interfaces

$[Fe(CN_6)^{3-/4-}]$ probed the electron transfer rate and catalytic properties of the interface after each fabrication step in cyclic voltammetry. The variations in redox peak current and peak-to-peak separation indicate the change in electron transfer at each fabrication step. The redox peak current of bare electrode Fig. 2 A(a) was increased radically after MXene deposition as revealed in Fig. 2 A(b) and the peak separation was shifted from 0.43 to 0.37 V that might be attributed to the excellent conductivity and abundant reactive functional groups of MXene interface [39]. Moreover, the immobilization of PDI-MXene hierarchal nano-adduct on electrode surface as revealed in Fig. 2 A(c) further enhanced the faradic response with decreased peak-to-peak separation (0.26 V). The increase

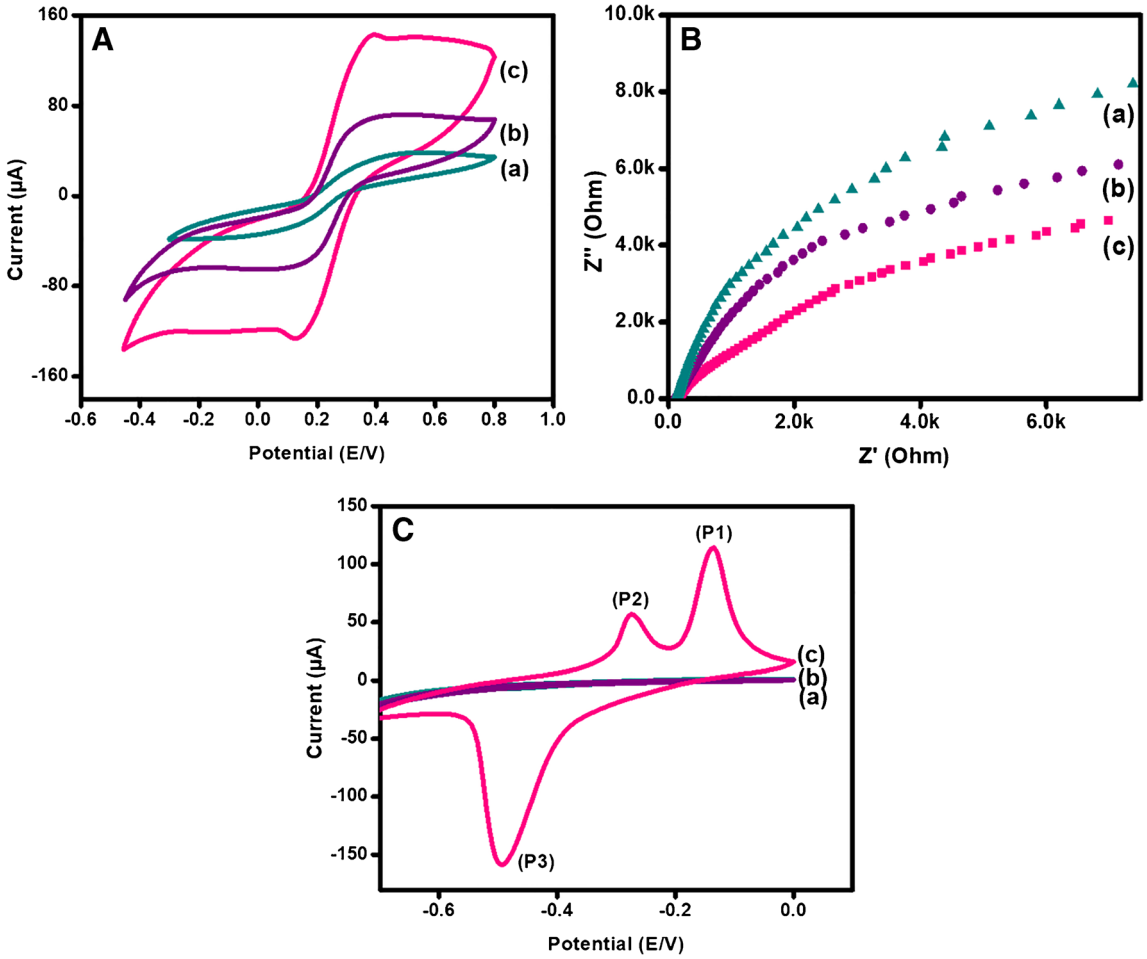

Fig. 2 Cyclic Voltammetric response (**A**) and electrochemical impedance spectroscopy (**B**) of bare GPE (a), modified with MXene (b) and PDI-MXene (c) in 5 mM $[Fe(CN)6]^{4-/3-}$ (1:1). Cyclic voltammetric response (**C**) of bare GPE (a), modified with MXene (b) and PDI-MXene (c) in the presence of 100 μM dopamine solution in phosphate buffer (pH=7.4). All the measurements were performed at a scan rate of 50 mVs^{-1}

in oxidation current (68.8 to 142.7 μA) and decreased redox peak separation could be accredited to stable and thin film formation with enhanced electrochemical active surface area possessed by nano-adduct [40]. Likewise, the electron-attracting dianions of PDI also contributed towards the amplification of faradic current.

Randles–Sevcik equation has been employed to premeditate the electrochemical active surface area (EASA) of the PDI-MXene/GPE from the peak current acquired by the cyclic voltammograms in $[Fe(CN)_6]^{3-/4-}$ (redox probe) [41].

$$i_p = 2.69 \times 10^5 A n^{3/2} D_{red}{}^{1/2} C^* \mathcal{V}^{1/2} \quad (1)$$

where "A" is electrochemical active surface area, "n" is the number of electrons involved in the oxidation or reduction of potassium ferro/ferricyanide, which in this current case is 1, "C*" is the concentration of ferrocyanide (5×10^{-3} M), "D_{red}" is the diffusion coefficient of potassium ferrocyanide (7.6×10^{-6} cm^2 s^{-1}), and "v" is the scan rate (50×10^{-3} V). The electrochemically active surface area of the MXene/GPE and PDI-MXene/GPE was calculated to be 0.05 cm^2 and 0.14 cm^2, respectively. The enhanced EASA of this integrated interface in comparison to its pristine materials corroborated the enhanced faradic current and greater electrocatalytic activity.

Electrochemical impedance spectroscopy (EIS) provided the information of the interfacial characteristics of electrodes in the form of a Nyquist plot during each fabrication stage. It revealed electron transfer parallel to a semicircle at higher frequencies along with diffusion-limited processes from linear portions at lower frequencies [42]. As envisioned from Fig. 2 (B), the charge transfer resistance of bare electrode (R_{ct} = 152 Ω) Fig. 2 B(a) was reasonably decreased after MXene deposition (R_{ct} = 130.6 Ω), as shown in Fig. 2 B(b). The consequent decrease in resistance was ascribed to enhanced electron transfer property possessed by material and results are in consistent with CV findings. However, an explicit decrease in resistance was observed after PDI-MXene deposition (R_{ct} = 109 Ω), as indicated in Fig. 2 B(c) which might be due to exotic electronic conductivity along with ideal stability possessed by nano-adduct. Likewise, the electron-attracting

amide group could also promote the electron transfer from the redox probe to the electrode interface. This desirable variation in the impedimetric response after modification of electrode surface with PDI-MXene nano-adduct indicates the fabrication of superior sensing surfaces with the enhanced active surface area for greater catalytic performance.

Furthermore, the proficiency of PDI-MXene toward an electrochemical determination of dopamine was evaluated. To accentuate the synthesis of nano-adduct as control experiments, bare GPE and electrodes modified with pristine materials were evaluated which displayed no peak in the presence of 100 μM dopamine, as shown in Fig. 2 C(a, b).

However, after modification of GPE with PDI-MXene, two oxidation peaks were observed in their spectra as shown in Fig. 2 C(c). In the CV spectra, a prominent peak named P1 at −0.135 V depicted the oxidation of DA to o-dopaminequinone (DAQ) after complexation with nano-adduct. Likewise, the reduction peak P3 at −0.495 V represented the conversion of DAQ back to DA. However, second oxidation peak P2 at −0.275 V was also observed, which probably indicates the conversion of DAQ to leucodopaminochrome (LDAC) due to intramolecular cyclization owing to Michael's addition that specifically takes place above pH 7 (7.4 in present case) in PBS [43, 44]. The stepwise conversion of this redox couple P2/P3 representing LDAC/DAC transitions has been detailed in scheme S1. The much larger cathodic peak current in contrast to anodic current corroborated the electrochemical reversibility of reaction [44–46] at the surface of PDI-MXene. Furthermore, the oxidation of DA at such a low potential sanctioned the superior electrocatalytic ability for DA oxidation to get enhanced EASA for fast electron transfer.

Reaction kinetics at integrated PDI-MXene/GPE interface

In order to study the electron transfer process along with reaction kinetics and surface activity at the PDI-MXene interface, cyclic voltammetry at different scan rates was performed Fig. 3 (A). The effect of scan rate on faradic current was plotted in the presence of 100 μM DA with the scan rates ranging from 5 to 150 mVs^{-1} as perceived from Fig. 3 (B). The redox peak current was increased with a subsequent increase in scan rate. Such response could be reasoned to the fact that at higher scan rates electrode surface gets more time and more exposure to the analyte that results in enhanced catalytic activity along with the greater faradic current. Moreover, a slight shift in potential with an increase in scan rate has also been observed due to the fast electron transfer process thus suggesting our mechanistic procedure is a surface-controlled process [47]. Additionally, the adsorption-controlled process at our integrated sensing interface is due to redox-active quinones and aromatic ring that lead to the fast shuttling of electrons at the electrode-electrolyte interface.

As illustrated in Scheme 1, MAX phase was exfoliated to form MXene. Later on, PDI was self-assembled on the 2D surface of the MXene substrate with the help of its surface functional groups and π-π stacking/H bonding. This interaction resulted in increased mechanical stability and surface defects that enhanced the sensitivity. These surface defects further enhanced DA adsorption rendering provision of more oxidation. Hence, with the increased electrocatalytic activity, this integrated interface could prove highly robust, sensitive, and selective for DA detection.

Sensing efficacy of integrated PDI-MXene/GPE interface towards DA

DPV was also employed to investigate the response of developed PDI-MXene/GPE sensor against different concentrations of DA owing to its well-defined current response, magnified resolution, lower background noise along, and capability to reduce non-faradic response [48]. The DPV findings as revealed in Fig. 4 (A and B) suggested the linear increment in faradic current with an increase in DA concentration [49].

Besides the current enhancement, a slight potential shift has also been witnessed in DPV that denotes the enhanced surface coverage and adsorption of dopamine at electrode interface with the increase in DA concentration [50, 51].

We further employed the amperometry that is capable of achieving lower detection limits owing to its increased current sensitivity along with its ability to reduce the non-faradic current. Hence, amperometric responses of PDI-MXene-modified electrodes in different concentrations of dopamine were obtained at −0.13 V of applied potential. The linear increment in faradic current was observed with increasing concentrations of DA. However, a lesser sensitivity at higher concentration (100 to 1000 μM) has been observed compared to lower concentrations as revealed from linear graphs of DPV and amperometry of Fig. 4 B&D. It can be credited to comparatively higher energy needed for anodic stripping and ohmic drop at higher concentrations as compared to lower concentrations [52]. These results manifest the analyte concentration dependence of as-fabricated electrodes for their electrocatalytic response, as shown in Fig. 4 (C). Briefly, the presence of accordion-like MXene stacks with ideal flake thickness of 95.6 nm enhanced the conductivity of interface and abundant reactive surface functional groups provided interconnecting points for further immobilization to generate a stable interface with enhanced sensitivity. Meanwhile, the rigid PDI infrastructure leverage increased electronic conjugation owing to π-π interactions between redox-active quinones and aromatic ring that lead to fast charge transport mobility at electrode-electrolyte interface thus promoting redox activity of DA with robust response (2 s), corroborating sensing efficacy in terms of excellent sensitivity (38.1 $\mu A \mu M^{-1} cm^{-2}$), detection limit (6.8 nM), and stability. The current obtained from

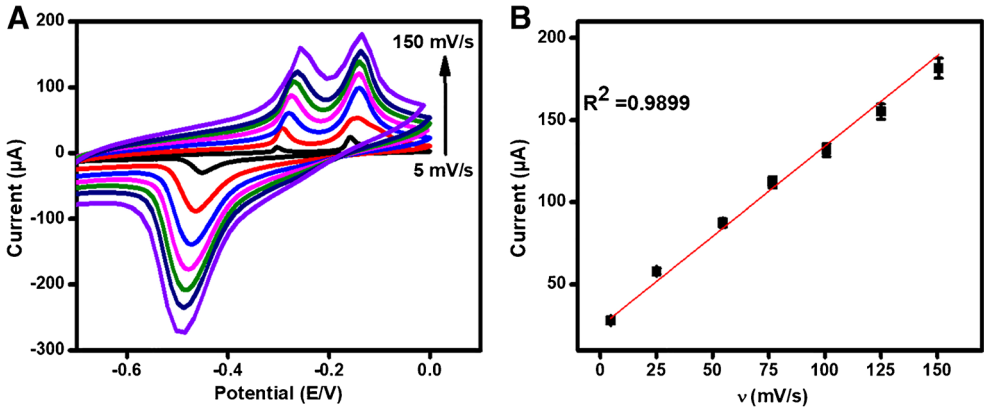

Fig. 3 Cyclic voltammetric response (**A**) and its corresponding linear graph (**B**) of PDI-MXene/GPE in the presence of 100 μM DA in phosphate buffer saline (pH 7.4) at different scan rates (5 to 150 mV/s)

amperometry and DPV was plotted against increasing concentrations of DA Fig. 3 (B and D), and the resultant plot presented two linearities, one in lower DA concentration range, i.e., 10 to 100 μM, and the second in higher DA concentration range, i.e., 100 to 10,000 μM. The wide linear range and superior detection limit in contrast to the literature show the improved analytical performance of as-fabricated sensor towards DA.

Surface coverage (Γ) of dopamine on the interface of synthesized adduct PDI-MXene /GPE can be calculated using the Lavirion equation.

$$I_p = \frac{n^2 F^2 A \Gamma \upsilon}{4RT} \quad (2)$$

where "n" indicates the number of transferred electrons (n=2), "F" and "A" represent the Faraday constant and area of the graphitic pencil electrode respectively, while "R" and "T" represent the general constants. The surface coverage of Dopamine on the working electrode interface was calculated to be 6.83×10^{-5} mol cm^{-2}. Higher surface coverage of DA explicates increased and fast electron transfer and authorizes the findings.

Antifouling property of integrated PDI-MXene/GPE interface

As a control experiment in order to emphasize the fouling and antifouling properties of modified interface, we immersed the modified electrode in concentrated solution of analyte (1000 μM of DA) for 10 min and was analyzed at same experimental conditions. The current signals of the electrode decreased as shown in fig S5 A(a) than those reported in Fig. 3(a). This decrease in performance is due to fouling of the electrode caused by DA and its derivatives that stick on electrode interface and form insulating layer which reduce the active surface area that lead to poor performance [53]. Nevertheless, the performance of the developed electrode can be regenerated after 5-min bath sonication in DI water as shown in fig S4 A(b). The linear relationship between oxidation current and DA concentration before and after sonication is shown in fig S5 B(a and b). Likewise, the DPV curves of the original, DA fouled in 1000 μM DA and electrode after 5 min sonication were also analyzed. The current peak of the fouled electrode fig S5 C(a) decreased to more than 30% than original electrode as shown in fig S5 C(b). Meanwhile, the developed surface after 5-min ultrasonic cleaning displayed almost the same level (only 0.5% in current change) as shown in fig S5 C(c). These results revealed that our integrated interface poses potential of ease of regeneration and antifouling abilities which carries potential for several applications.

Selectivity, repeatability, reproducibility, and stability of integrated PDI-MXene/GPE interface

To inspect the practical application of the developed electrochemical sensor, selectivity is the main representative feature. Therefore, the response of transducing interface was analyzed in the presence of interfering species as they coexist with DA in the extracellular fluid. In Fig. 5 (A), a prominent faradic current can be envisioned after the addition of 100 μM DA; however, a lesser response was recorded after the addition of 1000 μM of each interferent. It shows the selectivity of our developed transducing surface towards DA, even in the presence of 10-fold excess of physiological interferents. The superior selectivity of PDI-MXene towards dopamine could be due to the π-π interaction of planner structure of nano-adduct and DA phenyl group resulting in easier electron transfer for DA oxidation. However, the interaction of nano-adduct with other interferents is weak that leads to inactive oxidation that is why a lower faradic response is observed. Moreover, the developed sensor did not even show a good response towards AA and UA as at pH 7.4, AA and UA have negative charges while DA is positively charged. Therefore, the negatively charged nitrogen atom of PDI attracts the positively charged DA and repels AA and UA [54].

The repeatability, reproducibility, and stability of the developed PDI-MXene/GPE were investigated and tested under

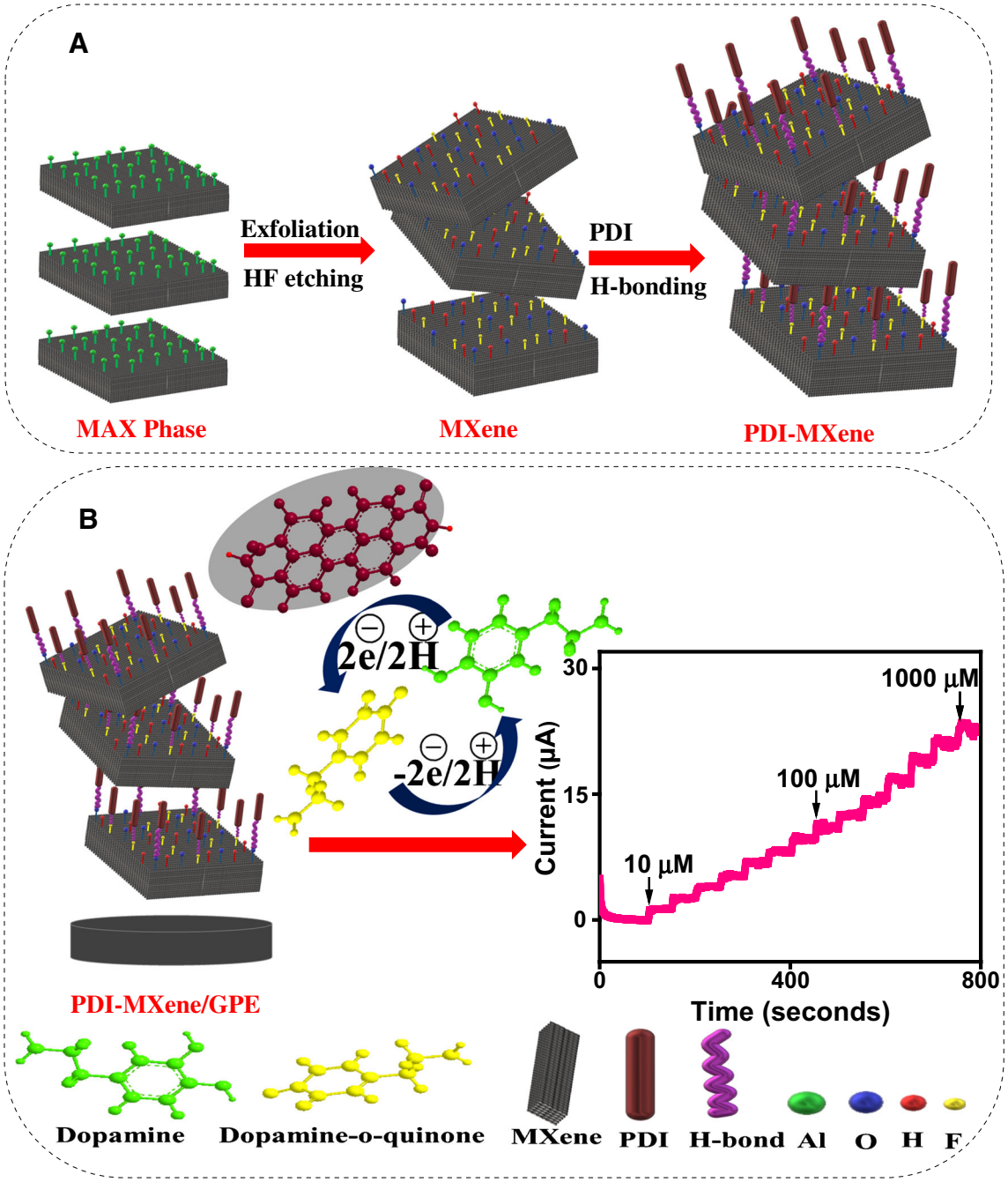

Scheme 1 Schematic illustration of the oxidative process involved on constructed sensing interface for the development of a non-enzymatic dopamine sensor

analogous analytical parameters to analyze its practical applicability. The relative standard deviation was calculated to be 1.90% after recurrent usage of the same fabricated electrode (n=10), indicating good precision and admirable repeatability of the developed sensor, as shown in Fig. 5 (B). Likewise, to assess the reproducibility of the fabricated sensor, the CV response of 6 paralleled electrodes was examined for DA sensing under similar conditions, as shown in Fig. 5 (C). The relative standard deviation, in this case, was found to be 1.52% consenting to an excellent reproducibility of the developed sensor. Similarly, the stability of the projected sensor was also evaluated by storing it at room temperature and subsequently analyzing it after every 7 days against DA Fig. 5 (D). The relative standard deviation was found to be 2.14% authorizing the long-term stability and reliability of the anticipated sensor.

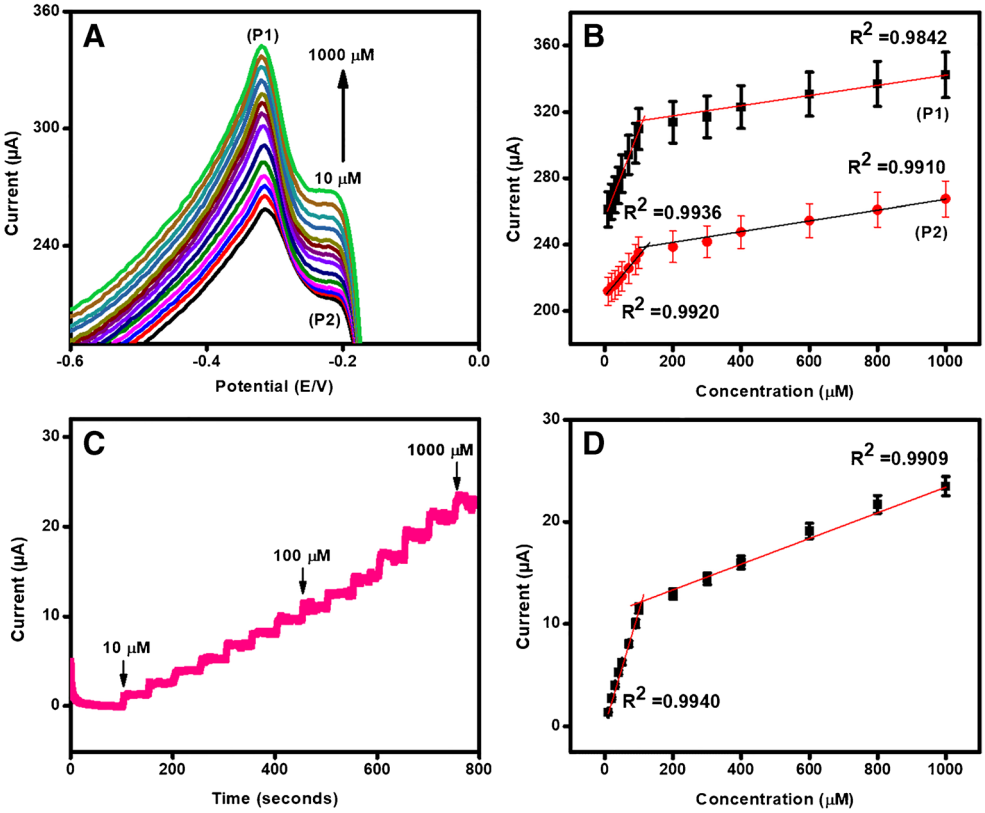

Fig. 4 Differential pulse voltammetric response (**A**) and its corresponding linear graph (**B**), and amperometric response (**C**) and its corresponding linear graph (**D**) for PDI-MXene/GPE at a concentration ranging from 10 to 1000 µM. All studies were performed in phosphate buffer saline (pH 7.4) at a scan rate of 50 mV/s

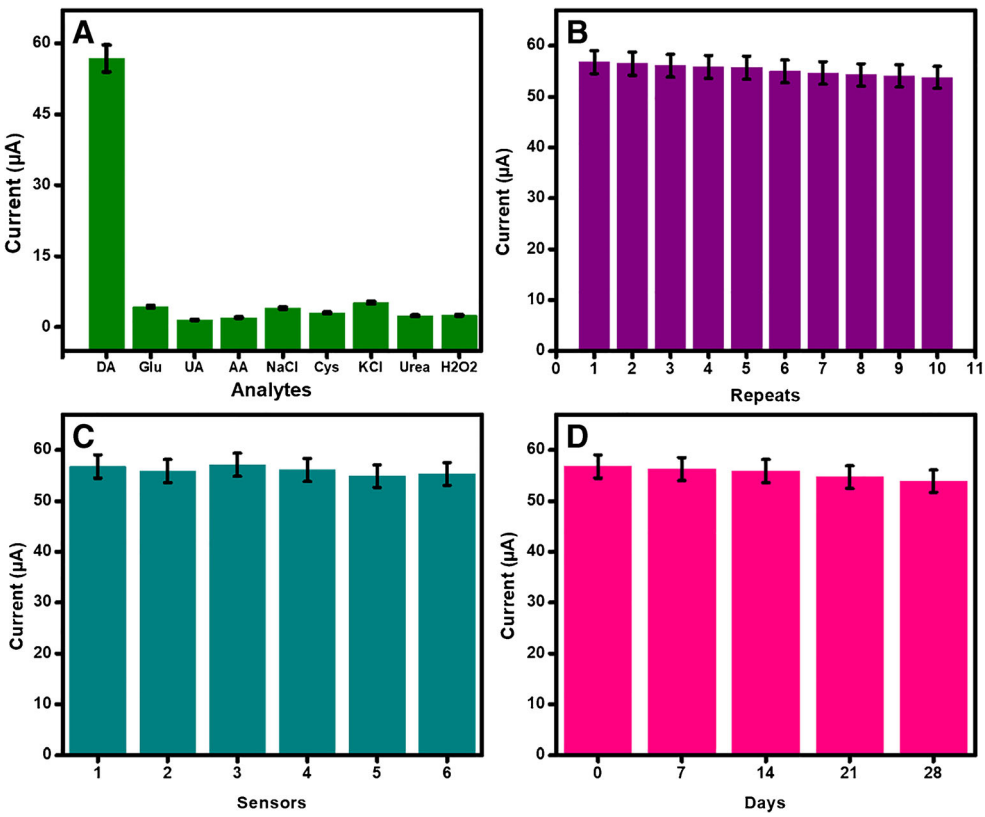

Fig. 5 Current response (**A**) of PDI-MXene/GPE in the presence of 100 µM DA and 1000 µM interfering species (glucose, uric acid, ascorbic acid, sodium chloride, cysteine, potassium chloride, urea, and hydrogen peroxide) in phosphate buffer saline (pH 7.4) at a scan rate of 50 mV/s. Repeatability (**B**) of PDI-MXene-modified GPE for their response towards DA for ten times. Reproducibility (**C**) of 6 GPE modified with PDI-MXene for their response towards DA under similar analytical parameters. Stability (**D**) of PDI-MXene-modified GPE for their response towards DA for 28 days

Table 1 The recovery statistics of the integrated sensor in human serum for dopamine sensing

Sample	Dopamine added (μM)	Dopamine found (μM)	Relative standard deviation % (n=3)	Relative error %	Recovery %
1	50	49.9	0.4	0.20	100.2
2	100	99.7	0.1	0.23	99.9
3	300	296	0.4	0.19	98.6

Real sample analysis on integrated PDI-MXene/GPE interface

Complex biological systems impose a stringent restriction on the practical development of electrochemical sensors as they are infatuated with many biological interferents other than DA. Therefore, the real sample analysis of the as-integrated sensing surface PDI-MXene/GPE was performed to analyze the practical analytical performance

Table 1 showed the recovery of DA at three different spiked concentrations (50 μM, 100 μM, and 300 μM) in PBS having pH 7.4. The procedure and recovery calculation method has been elaborated in supporting information [55, 56]. The recoveries were found in the range of 98.6 to 100.2%, as shown in Table 1. Moreover, the standard addition method was applied to serum samples to investigate the selectivity properties of designed electrochemical sensor. Calibration equation of standard addition method is found to be y (μA) = 0.11× (μM) + 0.22. These excellent recoveries of the DA in spiked samples validate the high accuracy of developed sensor in complex medium.

Moreover, the findings of the integrated dopamine sensor were evaluated and compared with conventional reported systems as displayed in Table 2. The good sensitivity, wide linear range, and lower detection limit along with maximum reproducibility made the as-fabricated interface an ideal platform for dopamine sensing. Moreover, lower working potential of the present fabricated sensor is the main plus point of the present study. However, there is still a great room in investigating the in vivo applications of MXene-based nanocomposites as well as to work on the poor stability of MXene and their composite materials.

Table 2 Comparison of dopamine analytical parameters obtained on different electrode matrixes found in recent literature with the as-fabricated interface

Electrode matrix	Sensitivity ($\mu A \mu M^{-1} cm^{-2}$)	LOD (nM)	Linear range (μM)	Reproducibility (RSD %)	Detection potential (V)	Ref.
PEDOT-LSG	0.220 ± 0.011	330	1–150	2.7	0.25	[57]
$SiO_2/C/Co_3O_4$	80	18	10–240	2.5	0.25	[58]
CB-GCE	0.61	60	0.1–20	–	0.14	[59]
GNPs/MWCNTs	2.06	70	0.4–5.7	–	0.16	[60]
Fe_3O_4-Gr/GCE	–	750	5.0-160	–	~ 0	[61]
GCE/N-rGO-180-8/NH_3	1.82	410	0.5–150.0	6.22	0.2	[62]
Ag@MoS_2/GCE	–	200	1–500	–	0.15	[63]
TiO_2/TiCT/NUF/GCE	9.2	0.2	0.002–100	069	0.144	[64]
ErGO/MWCNTs/PPy	8.96	2.3	0.025–1	5.43	0.25	[65]
$Ti_3C_2T_x$	–	3	0.015–10	1.14	0.245	[66]
Ti_3C_2/DNA/Pd/Pt@GCE	1.05	30	0.2–1000	–	~ 0.2	[67]
CuO/CeO_2/SPCE	4.823	16	0.025–98.5	3.72	~ 0.3	[68]
RuS_2 /GCE	1.8	73.8	10–80	6.4	0.25	[69]
PDI-MXene/GPE	38.1	240	10–100 100–1000	1.52	−0.135	This work

PEDOT-LSG poly(3,4-ethylenedioxythiophene)-modified laser-scribed graphene; *$SiO_2/C/Co_3O_4$* carbon ceramic electrode of SiO_2/C modified with Co_3O_4 nanoparticles; *CB* carbon black; *GNPs/MWCNTs* gold nanoparticles supported on multi-walled carbon nanotubes; *GR* graphene, *GCE* glassy carbon electrode; *N-rGOs* N-doped reduced graphene oxides; *Ag@MoS2/GCE* molybdenum disulfide nanosheet decorated with silver nanoparticles; *CuO/CeO2/SPCE* copper oxide, cerium oxide, screen-printed carbon electrode; *RuS_2* ruthenium(IV) disulfide

Conclusion

The paper reports the fabrication of a PDI-MXene/GPE-based electrochemical dopamine sensor. The developed interface proved to be a simple, robust, miniaturized, and highly efficient transducing site for DA oxidation at lower potential with ultra-sensitivity and enhanced selectivity even in the presence of biological interfering analytes. The higher EASA along with increased DA coverage on electrode interface owing to the synergistic effect of MXene and PDI leads to superior analytical performance. The achieved detection limit and wider linear ranges are a result of an integrated system with minute perturbations and low ohmic resistance. The developed interface also proved to be effective even in real samples with considerable sensitivity and selectivity, implying the great potential for diverse practical applications in the biomedical field.

Supplementary Information The online version contains supplementary material available at https://doi.org/10.1007/s00604-021-04884-0.

Funding MHN received financial supports provided by HEC (20-4993/R&D/HEC/14/614) and CUI (16-14/CRGP/CIIT/LHR/15/776).

Compliance with ethical standards

Conflict of interest The authors declare that they have no competing interests.

References

1. Xu S, Dall'Agnese Y, Wei G, Zhang C, Gogotsi Y, Han W (2018) Screen-printable microscale hybrid device based on MXene and layered double hydroxide electrodes for powering force sensors. Nano Energy 50:479–488
2. Huang Q, et al. (2020) Graphene quantum dots/multiwalled carbon nanotubes composite-based electrochemical sensor for detecting dopamine release from living cells. ACS Sustainable Chemistry & Engineering
3. Shapiro MG, Westmeyer GG, Romero PA, Szablowski JO, Küster B, Shah A, Otey CR, Langer R, Arnold FH, Jasanoff A (2010) Directed evolution of a magnetic resonance imaging contrast agent for noninvasive imaging of dopamine. Nat Biotechnol 28(3):264–270
4. Belujon P, Grace AA (2017) Dopamine system dysregulation in major depressive disorders. Int J Neuropsychopharmacol 20(12): 1036–1046
5. Huang C-W, Lu MS-C (2011) Electrochemical detection of the neurotransmitter dopamine by nanoimprinted interdigitated electrodes and a CMOS circuit with enhanced collection efficiency. IEEE Sensors J 11(9):1826–1831
6. Yang J, Hu Y, Li Y (2019) Molecularly imprinted polymer-decorated signal on-off ratiometric electrochemical sensor for selective and robust dopamine detection. Biosens Bioelectron 135:224–230
7. Li R, Liang H, Zhu M, Lai M, Wang S, Zhang H, Ye H, Zhu R, Zhang W (2021) Electrochemical dual signal sensing platform for the simultaneous determination of dopamine, uric acid and glucose based on copper and cerium bimetallic carbon nanocomposites. Bioelectrochemistry 139:107745
8. Savk A, Özdil B, Demirkan B, Nas MS, Calimli MH, Alma MH, Inamuddin, Asiri AM, Şen F (2019) Multiwalled carbon nanotube-based nanosensor for ultrasensitive detection of uric acid, dopamine, and ascorbic acid. Mater Sci Eng C 99:248–254
9. Umapathi S et al (2020) Electrochemical sensor based on CuSe for determination of dopamine. Microchim Acta 187(8):1–13
10. Jiang Q, Kurra N, Alhabeb M, Gogotsi Y, Alshareef HN (2018) All pseudocapacitive MXene-RuO2 asymmetric supercapacitors. Adv Energy Mater 8(13):1703043
11. Wang Z, Xu Z, Huang H, Chu X, Xie Y, Xiong D, Yan C, Zhao H, Zhang H, Yang W (2020) Unraveling and Regulating Self-Discharge Behavior of Ti3C2T x MXene-Based Supercapacitors. ACS Nano 14(4):4916–4924
12. Chen WY et al (2020) Nanohybrids of a MXene and transition metal dichalcogenide for selective detection of volatile organic compounds. Nat Commun 11(1):1–10
13. Chertopalov S, Mochalin VN (2018) Environment-sensitive photoresponse of spontaneously partially oxidized Ti3C2 MXene thin films. ACS Nano 12(6):6109–6116
14. Lyu B, Kim M, Jing H, Kang J, Qian C, Lee S, Cho JH (2019) Large-area MXene electrode array for flexible electronics. ACS Nano 13(10):11392–11400
15. Chen Y, Ge Y, Huang W, Li Z, Wu L, Zhang H, Li X (2020) Refractive index sensors based on Ti3C2Tx MXene fibers. ACS Applied Nano Materials 3(1):303–311
16. Ma Y, Liu N, Li L, Hu X, Zou Z, Wang J, Luo S, Gao Y (2017) A highly flexible and sensitive piezoresistive sensor based on MXene with greatly changed interlayer distances. Nat Commun 8(1):1207
17. Maleski K, Mochalin VN, Gogotsi Y (2017) Dispersions of two-dimensional titanium carbide MXene in organic solvents. Chem Mater 29(4):1632–1640
18. Enyashin AN, Ivanovskii AL (2013) Structural and electronic properties and stability of MX enes Ti2C and Ti3C2 functionalized by methoxy groups. J Phys Chem C 117(26):13637–13643
19. Zhu P, Wang Y, Ma P, Li S, Fan F, Cui K, Ge S, Zhang Y, Yu J (2019) Low-power and high-performance trimethylamine gas sensor based on nn heterojunction microbelts of perylene diimide/CdS. Anal Chem 91(9):5591–5598
20. Amara U, Mahmood K, Riaz S, Nasir M, Hayat A, Hanif M, Yaqub M, Han D, Niu L, Nawaz MH (2021) Self-assembled perylene-tetracarboxylic acid/multi-walled carbon nanotube adducts based modification of screen-printed interface for efficient enzyme immobilization towards glucose biosensing. Microchem J 165:106109
21. Li G, Zhao Y, Li J, Cao J, Zhu J, Sun XW, Zhang Q (2015) Synthesis, characterization, physical properties, and OLED application of single BN-fused perylene diimide. The Journal of organic chemistry 80(1):196–203
22. Schuster NJ, Paley DW, Jockusch S, Ng F, Steigerwald ML, Nuckolls C (2016) Electron delocalization in perylene diimide helicenes. Angew Chem Int Ed 55(43):13519–13523
23. Aulin YV, Felter KM, Günbas DD, Dubey RK, Jager WF, Grozema FC (2018) Morphology-independent efficient singlet exciton fission in perylene diimide thin films. ChemPlusChem 83(4): 230–238
24. Yip AMH, Shum J, Liu HW, Zhou H, Jia M, Niu N, Li Y, Yu C, Lo KKW (2019) Luminescent rhenium (I)–polypyridine complexes appended with a perylene diimide or benzoperylene monoimide moiety: photophysics, intracellular sensing, and photocytotoxic activity. Chem Eur J 25(38):8970–8974

25. Zou G, Zhang Z, Guo J, Liu B, Zhang Q, Fernandez C, Peng Q (2016) Synthesis of MXene/Ag composites for extraordinary long cycle lifetime lithium storage at high rates. ACS Appl Mater Interfaces 8(34):22280–22286
26. Lorencova L, Bertok T, Filip J, Jerigova M, Velic D, Kasak P, Mahmoud KA, Tkac J (2018) Highly stable Ti3C2Tx (MXene)/Pt nanoparticles-modified glassy carbon electrode for H2O2 and small molecules sensing applications. Sensors Actuators B Chem 263: 360–368
27. Riaz S et al (2016) Sonication-induced self-assembly of polymeric porphyrin–fullerene: Formation of nanorings. J Appl Polym Sci: 133(24)
28. Pu J-H, Zhao X, Zha XJ, Li WD, Ke K, Bao RY, Liu ZY, Yang MB, Yang W (2020) A strain localization directed crack control strategy for designing MXene-based customizable sensitivity and sensing range strain sensors for full-range human motion monitoring. Nano Energy 74:104814
29. Han M, Yin X, Wu H, Hou Z, Song C, Li X, Zhang L, Cheng L (2016) Ti3C2 MXenes with modified surface for high-performance electromagnetic absorption and shielding in the X-band. ACS Appl Mater Interfaces 8(32):21011–21019
30. Ali A et al (2016) Transparent and conductive Ti 3 C 2 T x (MXene) thin film fabrication by electrohydrodynamic atomization technique. J Mater Sci Mater Electron 27(5):5440–5445
31. Ling Z, Ren CE, Zhao MQ, Yang J, Giammarco JM, Qiu J, Barsoum MW, Gogotsi Y (2014) Flexible and conductive MXene films and nanocomposites with high capacitance. Proc Natl Acad Sci 111(47):16676–16681
32. Yang Y, Shi L, Cao Z, Wang R, Sun J (2019) Strain sensors with a high sensitivity and a wide sensing range based on a Ti3C2Tx (MXene) nanoparticle–nanosheet hybrid network. Adv Funct Mater 29(14):1807882
33. Kim SJ, Koh HJ, Ren CE, Kwon O, Maleski K, Cho SY, Anasori B, Kim CK, Choi YK, Kim J, Gogotsi Y, Jung HT (2018) Metallic Ti3C2T x MXene gas sensors with ultrahigh signal-to-noise ratio. ACS Nano 12(2):986–993
34. Lorencova L, Bertok T, Dosekova E, Holazova A, Paprckova D, Vikartovska A, Sasinkova V, Filip J, Kasak P, Jerigova M, Velic D, Mahmoud KA, Tkac J (2017) Electrochemical performance of Ti3C2Tx MXene in aqueous media: towards ultrasensitive H2O2 sensing. Electrochim Acta 235:471–479
35. Li X, Yin X, Han M, Song C, Xu H, Hou Z, Zhang L, Cheng L (2017) Ti 3 C 2 MXenes modified with in situ grown carbon nanotubes for enhanced electromagnetic wave absorption properties. J Mater Chem C 5(16):4068–4074
36. Soundiraraju B, George BK (2017) Two-dimensional titanium nitride (Ti2N) MXene: synthesis, characterization, and potential application as surface-enhanced Raman scattering substrate. ACS Nano 11(9):8892–8900
37. Zhao H, Zhang YY, Xu H, He EF, Zhang ZL, Peng QM, Zhang RJ, Zhang HQ (2015) Perylene diimide dye/layered carbide charge transfer composite: design, synthesis, and photophysical properties. Mater Lett 161:208–211
38. Suram SK, Newhouse PF, Gregoire JM (2016) High throughput light absorber discovery, part 1: an algorithm for automated tauc analysis. ACS Comb Sci 18(11):673–681
39. Zhang Y, Jiang X, Zhang J, Zhang H, Li Y (2019) Simultaneous voltammetric determination of acetaminophen and isoniazid using MXene modified screen-printed electrode. Biosens Bioelectron 130:315–321
40. Varol TÖ et al (2019) Fabrication of graphene/azobenzene-perylene diimide derivative modified electrochemical sensors for the dopamine detection based on full factorial experimental design. Measurement 147:106867
41. Purushothama H, Nayaka YA (2017) Electrochemical study of hydrochlorothiazide on electrochemically pre-treated pencil graphite electrode as a sensor. Sensing and bio-sensing research 16:12–18
42. Lee S-K, Song MJ, Kim JH, Kan TS, Lim YK, Ahn JP, Lim DS (2014) 3D-networked carbon nanotube/diamond core-shell nanowires for enhanced electrochemical performance. NPG Asia Materials 6(7):e115–e115
43. Ejaz A, Joo Y, Jeon S (2017) Fabrication of 1, 4-bis (aminomethyl) benzene and cobalt hydroxide@ graphene oxide for selective detection of dopamine in the presence of ascorbic acid and serotonin. Sensors Actuators B Chem 240:297–307
44. Hsu M-S, Chen YL, Lee CY, Chiu HT (2012) Gold nanostructures on flexible substrates as electrochemical dopamine sensors. ACS Appl Mater Interfaces 4(10):5570–5575
45. Li J, Jiang J, Xu Z, Liu M, Feng H, Liu Y, Qian D (2017) Synthesis of a nanocomposite consisting of Cu 2 O and N-doped reduced graphene oxide with enhanced electrocatalytic activity for amperometric determination of diethylstilbestrol. Microchim Acta 184(11): 4331–4339
46. Ning J, He Q, Luo X, Wang M, Liu D, Wang J, Liu J, Li G (2018) Rapid and sensitive determination of vanillin based on a glassy carbon electrode modified with Cu2O-electrochemically reduced graphene oxide nanocomposite film. Sensors 18(9):2762
47. He W, Liu R, Zhou P, Liu Q, Cui T (2020) Flexible micro-sensors with self-assembled graphene on a polyolefin substrate for dopamine detection. Biosens Bioelectron 167:112473
48. Mercante LA, Pavinatto A, Iwaki LEO, Scagion VP, Zucolotto V, Oliveira ON Jr, Mattoso LHC, Correa DS (2015) Electrospun polyamide 6/poly (allylamine hydrochloride) nanofibers functionalized with carbon nanotubes for electrochemical detection of dopamine. ACS Appl Mater Interfaces 7(8):4784–4790
49. Ramachandran R, Leng X, Zhao C, Xu ZX, Wang F (2020) 2D siloxene sheets: A novel electrochemical sensor for selective dopamine detection. Appl Mater Today 18:100477
50. Reddy S, Swamy BK, Jayadevappa H (2012) CuO nanoparticle sensor for the electrochemical determination of dopamine. Electrochim Acta 61:78–86
51. Hobbs CN, Johnson JA, Verber MD, Mark Wightman R (2017) An implantable multimodal sensor for oxygen, neurotransmitters, and electrophysiology during spreading depolarization in the deep brain. Analyst 142(16):2912–2920
52. Prasad BB, Jauhari D, Tiwari MP (2013) A dual-template imprinted polymer-modified carbon ceramic electrode for ultra trace simultaneous analysis of ascorbic acid and dopamine. Biosens Bioelectron 50:19–27
53. Yuan Q, Liu Y, Ye C, Sun H, Dai D, Wei Q, Lai G, Wu T, Yu A, Fu L, Chee KWA, Lin CT (2018) Highly stable and regenerative graphene–diamond hybrid electrochemical biosensor for fouling target dopamine detection. Biosens Bioelectron 111:117–123
54. Ören T, Birel Ö, Anık Ü (2018) Electrochemical determination of dopamine using a novel perylenediimide-derivative modified carbon paste electrode. Anal Lett 51(11):1680–1693
55. Yola ML (2021) Sensitive sandwich-type voltammetric immunosensor for breast cancer biomarker HER2 detection based on gold nanoparticles decorated Cu-MOF and Cu 2 ZnSnS 4 NPs/Pt/gC 3 N 4 composite. Microchim Acta 188(3):1–13
56. Karaman C et al (2021) Electrochemical immunosensor development based on core-shell high-crystalline graphitic carbon nitride@carbon dots and Cd 0.5 Zn 0.5 S/d-Ti 3 C 2 T x MXene composite for heart-type fatty acid–binding protein detection. Microchim Acta 188(6):1–15
57. Xu G, Jarjes ZA, Desprez V, Kilmartin PA, Travas-Sejdic J (2018) Sensitive, selective, disposable electrochemical dopamine sensor based on PEDOT-modified laser scribed graphene. Biosens Bioelectron 107:184–191

58. Younus AR, Iqbal J, Muhammad N, Rehman F, Tariq M, Niaz A, Badshah S, Saleh TA, Rahim A (2019) Nonenzymatic amperometric dopamine sensor based on a carbon ceramic electrode of type SiO 2/C modified with Co 3 O 4 nanoparticles. Microchim Acta 186(7):471
59. Jiang L, Nelson GW, Abda J, Foord JS (2016) Novel modifications to carbon-based electrodes to improve the electrochemical detection of dopamine. ACS Appl Mater Interfaces 8(42):28338–28348
60. Caetano FR, Felippe LB, Zarbin AJG, Bergamini MF, Marcolino-Junior LH (2017) Gold nanoparticles supported on multi-walled carbon nanotubes produced by biphasic modified method and dopamine sensing application. Sensors Actuators B Chem 243:43–50
61. Venkataprasad G, Madhusudana Reddy T, Lakshmi Narayana A, Hussain OM, Shaikshavali P, Venu Gopal T, Gopal P (2019) A facile synthesis of Fe3O4-Gr nanocomposite and its effective use as electrochemical sensor for the determination of dopamine and as anode material in lithium ion batteries. Sensors Actuators A Phys 293:87–100
62. Wiench P, González Z, Menéndez R, Grzyb B, Gryglewicz G (2018) Beneficial impact of oxygen on the electrochemical performance of dopamine sensors based on N-doped reduced graphene oxides. Sensors Actuators B Chem 257:143–153
63. Sookhakian M, Basirun WJ, Goh BT, Woi PM, Alias Y (2019) Molybdenum disulfide nanosheet decorated with silver nanoparticles for selective detection of dopamine. Colloids Surf B: Biointerfaces 176:80–86
64. Lu X et al (2021) A covalent organic polymer–TiO 2/Ti 3 C 2 heterostructure as nonenzymatic biosensor for voltammetric detection of dopamine and uric acid. Microchim Acta 188(3):1–11
65. Kathiresan V et al (2021) A simple one-step electrochemical deposition of bioinspired nanocomposite for the non-enzymatic detection of dopamine. Journal of Analytical Science and Technology 12(1):1–10
66. Shahzad F, Iqbal A, Zaidi SA, Hwang SW, Koo CM (2019) Nafion-stabilized two-dimensional transition metal carbide (Ti3C2Tx MXene) as a high-performance electrochemical sensor for neurotransmitter. J Ind Eng Chem 79:338–344
67. Zheng J, Wang B, Ding A, Weng B, Chen J (2018) Synthesis of MXene/DNA/Pd/Pt nanocomposite for sensitive detection of dopamine. J Electroanal Chem 816:189–194
68. Chen T-W, Chinnapaiyan S, Chen SM, Ali MA, Elshikh MS, Mahmoud AH (2020) A feasible sonochemical approach to synthesize CuO@ CeO2 nanomaterial and their enhanced non-enzymatic sensor performance towards neurotransmitter. Ultrason Sonochem 63:104903
69. Deepika J, Sha R, Badhulika S (2019) A ruthenium (IV) disulfide based non-enzymatic sensor for selective and sensitive amperometric determination of dopamine. Microchim Acta 186(7):480